The Growth Mechanism of TiN Reaction Layers produced on AlN via Active Metal Bonding

Nobuyuki Terasaki[a,c*], Moe Sakaguchi[b], Hajime Chiba[b], Touyou Ohashi[a], Yoshiyuki Nagatomo[a], Yoshirou Kuromitsu[a], Tohru Sekino[c], Kevin M. Knowles[d]

[a] Central Research Institute, Mitsubishi Materials Corporation, Saitama 330-8508, Japan

[b] Central Research Institute, Mitsubishi Materials Corporation, Ibaraki 311-0102, Japan

[c] SANKEN (The Institute of Scientific and Industrial Research), Osaka University, 8-1 Mihogaoka, Ibaraki, Osaka 567-0047, Japan

[d] Department of Materials Science and Metallurgy, University of Cambridge, 27 Charles Babbage Road, Cambridge, CB3 0FS, UK

* Corresponding author

E-mail address: terasaki@mmc.co.jp

Abstract

Interfacial reactions related to the TiN layer growth process between nanocrystalline epitaxial layers of AlN deposited on *c*-plane sapphire and a Ti–containing metal brazing or sintering layer using Ag–Cu–TiH_2, Ag–TiH_2 and Cu–TiH_2 pastes have been investigated. The brazed/sintered samples were heated in vacuum at 850 °C for 30 min. The TiN layer produced at the metal/AlN interfaces consists of TiN particles < 50 nm in size and grain boundary phases including Al-containing Ag and Al-containing Cu. The Al concentration within the TiN layer decreases as the distance increases from the AlN epitaxial layer. These experimental observations all suggest that when AlN is used as a starting material in the active metal bonding method, interfacial reaction processes take place with the generation of a local Al-based eutectic liquid phase and elemental transport through this eutectic liquid phase.

1. Introduction

Renewable energy sources such as solar energy and wind energy do not emit carbon dioxide as a greenhouse gas. Therefore, they are important sources of electricity for achieving a low-carbon society. High-voltage direct current (HVDC) transmission, which has a higher transmission efficiency than alternating current (AC) transmission, can easily help to connect renewable generation systems such as solar energy and off-shore wind energy to the grid. An increased use of HVDC is therefore expected in the coming years to increase the efficient use of these renewable energy sources [1-3].

Since AlN has a low electrical conductivity and a high thermal conductivity [4-6], copper (Cu)–bonded aluminum nitride (AlN) substrates are suitable for the AC/DC conversion modules required to interface HVDC technology to the AC electricity network used by consumers. These modules are composed of high-voltage and large-capacity power semiconductor chips used in HVDC transmission systems.

Cu–bonded AlN substrates are produced industrially using active metal bonding (AMB) with Ag–Cu–Ti eutectic alloys as the bonding material and Ti as the active metal [7-10]. The AMB method is a liquid-state bonding process in which a Ag–Cu eutectic-based brazing alloy containing a highly reactive element such as Ti, Zr and Hf, which are called the active metal, can wet a chemically inert ceramic surface. The interfacial structure between Cu and AlN consists of a Ag–Cu eutectic alloy layer adjacent to the Cu and a titanium nitride (TiN) layer adjacent to the AlN. Most importantly, a good Cu/AlN interface always has a continuous TiN layer [11]. The formation of the TiN layer at the Cu/AlN interface is a consequence of the following chemical reaction:

$$Ti_{diss} + AlN \rightarrow TiN + Al_{diss} \quad (1)$$

In this reaction, AlN and TiN are in the solid state whereas Ti_{diss} and Al_{diss} are dissolved in the Ag–Cu eutectic liquid phase [12]. The Gibbs free energy for this reaction is negative above the Ag–Cu eutectic point (780 °C) [13, 14]. Generally, in the AMB method, an active intermetallic compound layer containing a ceramic component is formed by an interfacial reaction between the active metal and the ceramic, i.e., a Ti–*X* phase (*X* = N, O, C) is formed at

the interface when using a brazing material containing Ti [7–10, 15–18]. Interestingly, Ag and Cu inclusions were detected in the TiN layer at the Cu/AlN part of the substrate/braze interface in the work on the wettability of AlN–based ceramics using Ag–Cu–Ti AMB alloys reported by Taranets et al.[19] and in the heat transfer characteristics of these reported by Sivaprahasam et al. [20], respectively. A model of the interfacial evolution for the Cu–metalized polycrystalline AlN substrate using Ag–Ti paste was proposed by Zhang et al. [21]. This is the same bonding method as in our recent work on AlN [11]. The key points of the model of Zhang et al. are that (i) the innermost reaction of TiN layer which occurs along the AlN grain boundaries is a consequence of a low diffusion activation energy for this process and (ii) the volume shrinkage arising from the formation of TiN facilitates the inward transport of the Ag–Cu–Ti liquid phase at the AlN grain boundaries. These mechanisms suggest that the formation of the TiN layer in active metal bonding is not just a simple substitution reaction, but instead a more dynamic interfacial reaction involving the metallic elements present in the bonding process. In the work reported here, we have investigated in detail the interfacial structures which occur at Ag–Cu–Ti/AlN, Ag–Ti/AlN and Cu–Ti/ AlN interfaces in order to clarify what happens to each metal component within the metal/substrate systems during the bonding process using a single crystal epitaxial AlN film as the AlN substrate.

2. Experimental method

In this work, Ag (D_{10} = 1.2 μm, D_{50} = 1.6 μm and D_{90} = 2.8 μm), Cu (D_{10} = 0.6 μm, D_{50} = 0.8 μm and D_{90} = 1.1 μm) and TiH_2 (D_{10} = 2.1 μm, D_{50} = 5.2 μm and D_{90} = 10.7 μm) powders were added to an organic medium containing α-terpineol (96%), 2,2,4-trimethyl-1, 3-pentanediol (98.5%), and polymethyl methacrylate and mixed using a mechanical mixer (ARE-250, THINKY) to produce the proprietary metal paste. D_{10}, D_{50} and D_{90} correspond to the 10^{th} percentile, 50^{th} percentile and 90^{th} percentile of a volume-based particle size, respectively. These metal powders have a purity of > 99.0 wt%. Their balances are almost C and O. The concentrations of impurities related to the present work in these metal powders by glow discharge mass spectrometry (GD–MS) are shown as Table 1. The concentrations of Cu and Al in Ag powder were both 0.3 wtppm and that of Ag and Al in Cu powder were 9.8 wtppm and

below the determination limit (< 0.01 wtppm), respectively. The impurity concentration of TiH_2 powder was higher than that of Ag and Cu powders. The concentration of Ag, Cu and Al were 61, 39 and 60 wtppm, respectively. TiH_2, which was available with powder smaller in particle size than Ti, was useful to improve the uniformity of the metal pastes. Ag–26.4 wt%Cu–4.4 wt%TiH_2, Ag–6.0 wt%TiH_2 and Cu–14.3 wt%TiH_2 pastes were applied onto a commercially available Al_2O_3 sapphire (0001) substrate (Φ 50.8 mm × 430 μm) upon which there was a 1 μm thick single crystal epitaxial AlN film as the AlN substrate (DOWA Electronics Materials Co., Ltd) using a screen-printing machine. The orientation relationship between the AlN film and the Al_2O_3 substrate was (0001) AlN // (0001) Al_2O_3, $[11\bar{2}0]$ AlN // $[1\bar{1}00]$ Al_2O_3, as observed in other studies [22, 23]. A cross-sectional bright field (BF) transmission electron microscopy (TEM) image of the AlN/ Al_2O_3 interface observed along the $[11\bar{2}0]$ AlN zone axis is shown in Fig. 1, together with electron diffraction patterns from the AlN and the Al_2O_3. Strain contrast due to a large lattice mismatch between AlN and Al_2O_3 (11.6 %) is observed around the AlN/Al_2O_3 interface. In addition, contrast due to the grain boundaries of the AlN film is observed along the direction perpendicular to the AlN/Al_2O_3 interface. This means that columnar crystals of AlN with a grain size of up to 400 nm grow in the AlN film. These AlN columnar crystals are much smaller than the grain size of the polycrystalline AlN substrates examined by Zhang et al. in [21]. It is reasonable to assume that the interfacial reaction between each paste and AlN is the same as when using Ti. This is because the dehydrogenation reaction of TiH_2 is completed at a heating temperature far lower than the Ag–Cu eutectic temperature (780 °C) [24]. The amounts of Ag, Cu and TiH_2 were ≈ 6.3, 2.4 and 0.4 mg/cm^2, respectively. From our previous work [11], it was anticipated that a continuous TiN layer would be formed at the metal/AlN interface for this amount of Ag and TiH_2. Furthermore, the ratio of Ag to Cu is almost that at the eutectic composition [13]. After drying the samples at 150 °C for 10 min in air, each sample was placed inside a vacuum furnace and brazed (sintered) at 850 °C for 30 min, with heating and cooling rates of 10 °C/ min.

Cross-sections of these samples were observed using scanning electron microscopy (SEM) before more detailed observations were undertaken by scanning transmission electron microscopy (STEM). Samples were mounted in an acrylic polymer at room temperature and polished using standard

metallographic techniques and an argon-based ion beam polisher (ArBlade 5000, Hitachi High-Tech). The microstructures of all samples were analyzed using SEM (GeminiSEM 500, Carl Zeiss AG), which were operated at 1.8 kV.

Thin sections of the metal/AlN interface for STEM analysis were prepared using a focused ion beam (FIB) instrument (Scios, Thermo Fisher Scientific). These sections were reduced to a thickness between 30 and 100 nm by the FIB. Elemental analysis of the thin sections was performed in a Titan G2 ChemiSTEM equipped with an energy dispersive X-ray spectroscopy (EDS) system (NSS7, Thermo Fisher Scientific) and a Talos F200X (Thermo Fisher Scientific) equipped with an EDS system (Super-X, Bruker), which were operated at 200 kV, respectively.

3. Results and Discussion

A secondary electron (SE) image of the Ag–Cu–TiH_2/AlN interface after brazing at 850 °C for 30 min is shown in Fig. 2. This brazing temperature is higher than the liquidus temperature of the Ag–Cu–TiH_2 system used in this work (≈ 837 °C). This suggests that this metal layer has completely melted at the brazing temperature. The broken line in this figure corresponds to the position of the interface between AlN and Al_2O_3. It can be seen that Cu–Ti intermetallic compounds (IMCs) such as Cu_2Ti (tetragonal, *Cmcm*, a = 7.988 Å, b = 4.458 Å, c = 4.397 Å) and Cu_4Ti (tetragonal, *Pnma*, a = 4.526 Å, b = 4.345 Å, c = 1.292 Å) [25] are widely dispersed in the metal layer. This layer is composed of Ag–rich and Cu–rich phases arising from the melting of the Ag–Cu–TiH_2 paste. The TiN (cubic, $Fm\bar{3}m$, a = 4.239 Å) [26] reaction layer grows in from the surface of the AlN toward the Al_2O_3 substrate and contains a large number of bright areas < 100 nm size.

High angle annular dark field (HAADF) image of the Ag–Cu–TiH_2/AlN interface together with elemental distributions are shown in Fig. 3. Bright areas between 40 nm and 200 nm in length which contain small particles are evident inside the TiN layer. These correspond to Ag and Cu–containing phases. Their presence suggests that the TiN layer growth process using AlN as a starting material via the AMB method cannot simply be expressed by the substitution reaction represented by equation (1). This implies that the Ag and/or Cu–containing liquid phase contributes significantly to the TiN layer growth process. HAADF images, dark field (DF) images and microdiffraction

patterns at each position on the Ti–containing metal layer side, center and the AlN side for the reaction layer at the Ag–Cu–TiH_2/AlN interface are shown in Fig. 4. These microdiffraction patterns are acquired from the yellow dotted circles inserted in Figs. 4(a1-6). These circles have a diameter, Φ, of ≈20 nm for Ag and ≈10 nm for Cu to analyze the Ag and Cu-containing phases independently. A larger beam diameter was used to help identify These DF images were taken under the beam condition with diffraction vectors ($\boldsymbol{g}$) shown in Figs.4(d1-6). It can be seen from these images that the TiN layer is composed of TiN, Ag (cubic, $Fm\bar{3}m$, a = 4.086 Å) and Cu (cubic, $Fm\bar{3}m$, a = 3.615 Å) at each position. These observations would suggest that the Ag–Cu liquid phase is intimately involved in the TiN growth process. Figs. 5(a, b) are obtained under the condition where the bright line evident in Fig. 5(a) is most sharp. Al from the AlN film appears to segregate together with Ag and Cu into the grain boundaries of the TiN layer, as shown by the line scan element analysis of Fig. 5(c) along the direction arrowed in Fig. 5(b). The concentrations of Ag, Cu and Al are 1.5, 22.5 and 5.3 at% at the peak position, respectively. It is suggested that these Ag or Cu–based spherical metal phases contain Al derived from AlN in the same way as the TiN grain boundary phases. In other words, the spherical metal phases in the TiN layer define the grain boundaries of the TiN layer. A detailed HAADF image of the TiN layer at the Ag–Cu–TiH_2/AlN interface is shown in Fig. 6. The TiN layer here is composed of TiN particles with < 50 nm size. Their grain boundaries contain Ag, Cu and Al as shown by the line scan element analysis in Fig. 5(c). Therefore, each TiN grain is surrounded by a metal-rich grain boundary phase which contains Ag, Cu and Al. This means that these metal grain boundary phases form a network structure over the entire TiN layer. In addition, the direction of observation of the TiN layer causes a difference in appearance of the bright areas shown in Figs. 5(a, b). Hence, a metal-rich grain boundary phase of the TiN layer is observed as a spherical metal phase in the TiN layer under the condition when it is observed from the direction almost parallel to its grain boundary.

SE images of (a) the Ag–TiH_2/AlN interface and (b) the Cu–TiH_2/AlN interface after sintering at 850 °C for 30 min are shown in Figs. 7(a, b), respectively. As in Fig. 2, the broken lines in these two figures correspond to the positions of the interface between AlN and Al_2O_3. In contrast to the fully dense Ag–Cu eutectic structure assisted by the Ag–Cu liquid phase

generation in Fig. 2, it is evident that there is porosity in both the Ag–rich and Cu–rich sinters. It is suggested that these porosity sinters are formed by insufficient void shrinkage between metal powders through solid phase sintering. In addition, there is a layer of TiC (cubic, $Fm\bar{3}m$, a = 4.328 Å) [27] and Cu–Ti IMCs clearly visible in Figs. 7(a, b), respectively. Since the surfaces of the Ag powder used in this work are covered with an organic medium, it is suggested that TiC is formed by the reaction with TiH_2 powder in contact with Ag powders during solid phase sintering. On the other hand, the Ag–rich phase densely precipitated as TiC particles formed locally at the Ag–Cu–TiH_2/AlN interface. It is suggested that the uneven distribution of TiC particles at the Ag–Cu–TiH_2/AlN interface is caused by the uneven distribution of the organic medium modifying the Ag particles and/or the convection of the Ag–Cu–Ti liquid phase. The details of Ag powder and TiC particles are shown in supplemental materials. It is significant that the heating temperature (850 °C) used for these sintering experiments is lower than the melting point of Ag (961.8 °C), Cu (1084.6 °C), Ti (1668 °C) and also the eutectic temperature of the Ag–Ti system (960 °C) [28] and the Cu–Ti system (875 °C) [25]. As with the Ag–Cu–TiH_2, the reaction layers between M–TiH_2 (M = Ag or Cu) and AlN grow in from the AlN surface toward the Al_2O_3 substrate. These layers contain a large number of bright areas < 100 nm size, similar to the size of Ag and Cu phases observed in the TiN layer as shown in Fig. 2.

A HAADF image of the Ag–TiH_2/AlN interface together with elemental distributions are shown in Fig. 8. It can be seen that the reaction layer is composed of the reactant containing Ti and N, and Ag phases which correspond to the bright area observed in Fig. 7(a). The size of the Ag phases in the reaction layer is about 10 % that of the Ag powder used in the Ag–TiH_2 paste. This implies that the generation of the Ag phase is completely different from the grain growth in the solid sintering process. That is, it means that the Ag–containing liquid phase is generated during the growth of the TiN layer. HAADF images, DF images and selected area electron diffraction (SAED) patterns at each position on the Ti–containing metal layer side, center and the AlN side for the reaction layer at the Ag–TiH_2/AlN interface are shown in Fig. 9. It can be seen that the reaction layer is composed of TiN and Ag (cubic) at each position from the SAED patterns as shown in Figs. 9(d1-3). In addition, the coincidence of the zone axes of TiN and Ag suggests

that there is an epitaxial orientation relationship between them as in the Ag–Cu–TiH_2/AlN interface.

A HAADF image of the Cu–TiH_2/AlN interface together with elemental distributions are shown in Fig. 10. The Cu phases which correspond to the bright area observed in Fig. 7(b) are distributed in the reaction layer mainly composed of the reactant containing Ti and N, as in the Ag–TiH_2/AlN interface. The size of Cu phase in the reaction layer is about 10 % of that of the Cu powder used in the Cu–TiH_2 paste. This also implies that the Cu phase in the Cu–TiH_2/AlN interfacial reaction layer is formed through the same reaction process as the Ag phase in the Ag–TiH_2/AlN interfacial reaction layer. HAADF images, DF images and SAED patterns at each position on the Ti–containing metal layer side, center and the AlN side for the reaction layer at the Cu–TiH_2/AlN interface are shown in Fig. 11. Here, the reaction layer is composed of TiN and Cu (cubic) at each position, as is evident from the SAED patterns shown in Figs. 11(d1-3). In addition, the coincidence of the zone axes of TiN and Cu suggests that there is an epitaxial orientation relationship between them as in the Ag–Cu–TiH_2/AlN interface.

These results show that the structural features of these TiN layers as shown Figs. 4, 9 and 11 do not depend on whether the Ti–containing metal layer is a liquid phase or a solid phase at the heat treatment temperature. This means that the formation reaction of the TiN layer using AlN as a starting material via the AMB method is composed of a TiN formation reaction by a substitution reaction and a local liquid phase formation reaction inside AlN.

The compositional analysis of the Ag and the Cu phases in the TiN layer for three samples are shown in Tables 2 and 3, which are obtained from each phase shown in Figs. 4, 9 and 11. In the Ag–Cu–TiH_2 system, the Al concentration with respect to the sum of the Ag, Cu and Al concentrations is also shown in parentheses in Tables 2 and 3. It can be seen that the Al concentration gradually decreases as the distance from the AlN increases. The implication is that the TiN grain boundaries function as diffusion paths and assist the transfer of elements between the Ti–containing metal layer and the AlN. It is notable that Al dissolves more in Cu than Ag in the Ag–Cu–TiH_2 system. In addition, the Al concentration dependence of the lattice constant of the Ag and the Cu phases in the TiN layer for three samples, which are estimated from the SAED patterns shown in Figs. 4, 9 and 11. It is

known that the lattice constants of these phases change linearly with respect to the Al concentration in the Al solid solution region [29–31]. The changes in these lattice constants estimated in this work lend further support to the proposition that there is a concentration gradient of *M* and Al in the TiN layer thickness direction.

Combining the results of the three sets of the interfacial reaction between Ti included metal layer and AlN, a formation mechanism of the TiN layer via the AMB method is proposed, as illustrated in Fig. 14. An interfacial reaction occurs between Ti in the Ti–containing metal layer and AlN according to the following chemical reaction:

$$Ti + AlN \rightarrow TiN + Al_{liq} \quad (2)$$

This substitution reaction causes the co-generation of TiN particles and the free Al liquid phase (Al_{liq}) on the AlN surface at temperatures above the Al melting point (660℃). In addition, there is an element *M* (*M* = Ag and/or Cu) that becomes eutectic with Al [32, 33] in the Ti–containing metal layer. Therefore, Al_{liq} immediately forms Al–M_{liq} as *M* dissolves in Al_{liq}, as shown below in equation (3), and shown schematically in Fig. 14(b). It is suggested that the Al–M_{liq} contributes to a lowering of the energy of the entire interfacial reaction system.

$$Al_{liq} + M \rightarrow Al\text{–}M_{liq} \quad (3)$$

It is further suggested that this Al–M_{liq} functions as a diffusion path for supplying Ti from the Ti–containing metal layer to the inside of AlN. This means that Ti newly reaching the AlN surface via these diffusion paths propagates the co-generation of TiN particles and the Al_{liq} into the inside of AlN by the chemical reaction (4), where Al_{liq} is immediately integrated with Al–M_{liq}. Furthermore, this means that the solidification reaction of Al–M_{liq} (5) proceeds simultaneously with the substitution reaction (4) due to the increase in the concentration of *M* in the Al–M_{liq} on the Ti–containing metal layer side since *M* also diffuses through these diffusion paths into the Al–M_{liq} as shown in Fig. 14(c).

$$Ti + AlN + Al\text{–}M_{liq} \rightarrow TiN + Al\text{–}M_{liq} \quad (4)$$

$$\mathrm{Al}\text{–}M_{\mathrm{liq}} + M \rightarrow M\text{–}\mathrm{Al}_{\mathrm{sol}} \quad (5)$$

Therefore, the substitution reaction (2) promotes the continuum of interfacial reactions between Ti–containing metal layer and AlN, and the TiN layer forming reaction proceeds inside the AlN by repeating the local reaction of equations (4) and (5), as shown schematically in Fig. 14(d). Consequently, the TiN layer is composed of TiN particles and grain boundaries with a concentration gradient of *M* and Al in the thickness direction of the TiN layer. This corresponds to a high *M* concentration on the Ti–containing metal layer side and a high Al concentration on the AlN side, respectively, as shown in Fig. 14(e). In the TiN formation reaction using AlN as a starting material via the AMB method, the local Al–M_{liq} plays an important role in the progress of the interfacial reaction between Ti–containing metal layer and AlN, and Al–M_{liq} and *M*–$\mathrm{Al}_{\mathrm{sol}}$ derive from this local liquid phase promote the transfer between Ti–containing metal layer and AlN as diffusion paths at all stages of the interfacial reaction.

4. Conclusions

Active metal bonding (AMB) has been applied industrially for bonding Cu onto AlN substrates since the 1990s**.** In this work, a growth mechanism of the TiN layer via the AMB method has been proposed from observations based on three sets of Ti–containing metal layer/AlN interfacial reactions. These are the Ag–Cu–TiH_2/AlN, Ag–TiH_2/AlN and Cu–TiH_2/AlN. In Ag–Cu–TiH_2/AlN, the TiN layer grown inside AlN at the Ag–Cu–TiH_2/AlN interface is composed of Ag and Cu grain boundary phases and TiN particles with < 50 nm size. In addition, Al from AlN segregates together with Ag and Cu into the TiN grain boundaries which surround the TiN particles. In the systems without a molten metal layer, such as Ag–TiH_2/AlN and Cu–TiH_2/AlN, the same structure of the TiN layer as with the Ag–Cu–TiH_2/AlN interface was observed. As the initiation reaction to form this characteristic TiN layer structure, the substitution reaction between Ti and AlN in contact with AlN (Eq. (2)) causes the co-generation of TiN particles and a Al liquid phase ($\mathrm{Al}_{\mathrm{liq}}$). Immediately, *M* (*M* =Ag and/or Cu) diffuses into $\mathrm{Al}_{\mathrm{liq}}$ to form the Al–M_{liq} (Eq.(3)), which provides diffusion paths for Ti toward the AlN surface. Furthermore, the Ti which has newly reached the AlN surface undergoes a

substitution reaction with AlN (Eq. (4)). Al–M_{liq} solidifies from the Ti–containing metal layer side to the AlN side because of the diffusion of M into Al–M_{liq}(Eq.(5)). This causes a concentration gradient of M and Al in the TiN layer thickness direction. The TiN layer grows into the AlN by a series of these local reactions.

References

[1] P. Bresesti, W. L. Kling, R. L. Hendriks, R. Vailati, HVDC connection of offshore wind farms to the transmission system, IEEE Transactions on Energy Conversion, 22, 2007, 37–43.

[2] C.-K. Kim, V. K. Sood, G.-S. Jang, S.-J. Lim, S.-J. Lee, HVDC Transmission: Power Conversion Applications in Power Systems, John Wiley & Sons Ltd., New York, 2009.

[3] J. Echeverria, S. Kouro, M. Pérez, H. Abu-rub, Multi-modular cascaded DC-DC converter for HVDC grid connection of large-scale photovoltaic power systems, Proceedings of IECON 2013, 39th Annual Conference of the IEEE Industrial Electronics Society, 2013, 6999–7005.

[4] M. Rahimo, A. Kopta, Switching to higher performance, ABB Review, issue no. 3, 2008, 19–24.

[5] D. Peters, B. Thomas, T. Duetemeyer, T. Hunger, R. Sommer, An experimental study of high voltage SiC PiN diode modules designed for 6.5 kV / 1 kA, Materials Science Forum, 679–680, 2011, 531–534.

[6] C. F. Bayer, E. Bär, B. Kallinger, P. Berwian, Thermal simulation of paralleled SiC PiN diodes in a module designed for 6.5 kV/1 kA, Materials Science Forum, 821–823, 2015, 616–619.

[7] H. Okamura, H. Shinohara, T. Funamoto, T. Shida, Bonding mechanism and microstructure of bonded zone of AlN ceramics with Ti-AgCu brazing metal, Quarterly Journal of the Japan Welding Society, 9(4), 1991, 494–501.

[8] Y. Nakao, K. Nishimoto, K. Saida, K. Murabe, Y. Fukaya, Microstructure of bonding layer in aluminum nitride to metals joints bonded by active brazing method, Quarterly Journal of the Japan Welding Society, 12(1), 1994, 115–121.

[9] Y. Nakao, K. Nishimoto, K. Saida, K. Murabe, Y. Fukaya, Bonding of aluminum nitride to copper for reducing thermal stress, Materials Transactions, JIM, 35(12), 1994, 910–916.

[10] D. Huh, D.-H. Kim, Joining of AlN to Cu using In-base active brazing fillers, Journal of Materials Research, 12(4), 1997, 1048–1055.
[11] N. Terasaki, T. Ohashi, Y. Nagatomo, Y. Kuromitsu, A. A. Shirzadi, A new method for liquid-phase bonding of copper plates to aluminum nitride (AlN) substrates used in high-power modules, Journal of Materials Science: Materials in Electronics, 30(7), 2019, 6552–6555.
[12] Q. Chen, B. Sundman, Thermodynamic assessment of the Ti–Al–N system. Journal of Phase Equilibria, 19(2), 1998, 146–153.
[13] M. W. Chase, JANAF thermochemical tables, 3rd ed., the American Chemical Society, and the American Institute of Physics for the National Bureau of Standards, 1986.
[14] P. R. Subrumanian, J. H. Perepezko, The Ag–Cu (Silver-Copper) system, Journal of Phase Equilibria, 14(1), 1993, 62–75.
[15] S. Kato, T. Yano, T. Iseki, Interfacial structures between Ag–Cu–Ti alloy and sintered SiC with various additives, Journal of the Ceramic Society of Japan, 101(3), 1993, 325–330.
[16] O. Saitoh, A. Suzumura, H. Ogawa, The corrosion phenomena of ruby by active metal brazing filler (Ag–Cu–Ti) at the brazing interface, Quarterly Journal of the Japan Welding Society, 14(4), 1996, 717–722.
[17] F.-L. Sun, J.-C. Feng, D. Li, Bonding of CVD diamond thick films using an Ag–Cu–Ti brazing alloy, Journal of Materials Processing Technology, 115(3), 2001, 333–337.
[18] M. Ali, K. M. Knowles, P. M. Mallinson, J. A. Fernie, Interfacial reactions between sapphire and Ag–Cu–Ti-based active brazed alloys, Acta Materialia, 103, 2016, 859–869.
[19] N. Yu. Taranets, H. Jones, Wettability of aluminum nitride based ceramics of different porosity by two active silver based brazing alloys, Materials Science and Engineering: A, 379(1–2), 2004, 251–257.
[20] D. Sivaprahasam, T. Sujitha, U. Gowtham, B. Jayachandran, R. Gopalan, Microstructure and heat transfer characteristics of active brazed ceramic–metal joints, Ceramics International, 47, 2021, 16133–16140.
[21] Y. Zhang, J. Zhang, J. Chen, Effect of interfacial microstructure evolution on the peeling strength and fracture of AMB Cu-metalized AlN substrate, Journal of the American Ceramic Society, 105, 2021, 577–589.
[22] Th. Kehagias, Ph. Komninou, G. Nouet, P. Ruterana, Th. Karakostas, Misfit relaxation of the AlN/Al_2O_3 (0001) interface, Physical Review B, 64,

2001, art. 195329.
[23] Y. Tokumoto, Y. Sato, T. Yamamoto, N. Shibata, Y. Ikuhara, Atomic structure of AlN/Al_2O_3 interfaces fabricated by pulsed-laser deposition, Journal of Materials Science, 41, 2006, 2553–2557.
[24] V. Bhosle, E. G. Baburaj, M. Miranova, K. Salama, Dehydrogenation of TiH_2, Materials and Engineering A, 356, 2003, 190–199.
[25] H. Okamoto, Cu–Ti (Copper-Titanium), Journal of Phase Equilibria, 23(6), 2002, 549–550.
[26] C. Vahlas, B. D. Ladouce, P. Y. Chevalier, C. Bernard, L. Vandenbulcke, A thermodynamic evaluation of the Ti–N system, Thermochimica Acta, 180, 1991, 23–37.
[27] H. Okamoto, Comment on C–Ti (Carbon-Titanium), Journal of Phase Equilibria, 16(6), 1995, 532–533.
[28] J. L. Murray, K. J. Bhansali, The Ag–Ti (Silver-Titanium) system, Bulletin of Alloy Phase Diagrams, 4(2), 1983, 178–183.
[29] I. Obinata, G. Wassermann, Röntgenographische Untersuchung der Löslichkeit von Aluminium in Kupfer, Naturwissenschaften, 21, 1933, 382–385.
[30] A. J. Bradley, H. J. Goldschmidt, X-ray study of slowly cooled iron-copper-aluminium alloys Part I. -Alloys rich in iron and copper, Journal of the Institute of Metals, 65, 1939, 389–401.
[31] W. B. Pearson, A Handbook of Lattice Spacings and Structures of Metals and Alloys, Pergamon Press, London, 1958.
[32] J. L. Murray, The aluminum–copper system, International Metals Reviews, 30(5), 1985, 211–233.
[33] A. J. McAlister, The Ag–Al (Silver-Aluminum) system, Bulletin of Alloy Phase Diagrams, 8(6), 1987, 526–533.

Caption list

Fig. 1 (a) A cross-sectional BF TEM image of the AlN/ Al_2O_3 interface observed along the [11$\bar{2}$0] AlN zone axis, as shown in (b) in the selected area electron diffraction pattern. (c) election diffraction pattern with the incident electron beam parallel to [11$\bar{2}$0] AlN// [1$\bar{1}$00] Al_2O_3.

Fig. 2 SE image of chemical reaction products at a Ag–Cu–TiH_2/AlN interface after brazing for 30 min at 850 °C.

Fig. 3 (a) HAADF image of a Ag–Cu–TiH_2/AlN interface after brazing for 30 min at 850 °C, together with elemental distributions of (b) Ti, (c) N, (d) Al, (e) Ag and (f) Cu obtained by energy dispersive X-ray spectroscopy (EDS).

Fig. 4 (a1-6) HAADF images of a Ag–Cu–TiH_2 /AlN interface after brazing for 30 min at 850 °C, (b1, 3, 5) DF images for Ag, (b2, 4, 6) for Cu and (c1-6) for TiN using $\boldsymbol{g}$ vectors as shown in (d1-6) micro diffraction patterns. These micro diffraction patterns were acquired from the yellow dotted circles shown in (a1-6).

Fig. 5 (a, b) HAADF images of a Ag–Cu–TiH_2/AlN interface after brazing for 30 min at 850 °C, and (c) EDS analysis along the direction arrowed in (b).

Fig. 6 Detailed HAADF image of TiN layer of a Ag–Cu–TiH_2/AlN interface after brazing for 30 min at 850 °C.

Fig. 7 SE images of chemical reaction products at (a) a Ag–TiH_2/AlN interface after sintering for 30 min at 850 °C, and (b) a Cu–TiH_2/AlN interface after sintering for 30 min at 850 °C.

Fig. 8 (a) HAADF image of a Ag–TiH_2/AlN interface after sintering for 30 min at 850 °C, together with elemental distributions of (b) Ti, (c) N, (d) Al and (e) Ag obtained by EDS.

Fig. 9 (a1-3) HAADF images of a Ag–TiH_2/AlN interface after sintering for 30 min at 850 °C, (b1-3) DF images for Ag and (c1-3) for TiN using $\boldsymbol{g}$ vectors

as shown in (d1-3) SAED patterns.

Fig. 10　(a) HAADF image of a Cu–TiH_2/AlN interface after sintering for 30 min at 850 °C, together with elemental distributions of (b) Ti, (c) N, (d) Al and (e) Cu obtained by EDS.

Fig. 11　(a1-3) HAADF images of a Cu–TiH_2/AlN interface after sintering for 30 min at 850 °C, (b1-3) DF image for Cu and (c1-3) for TiN using $\boldsymbol{g}$ vectors as shown in (d1-3) SAED patterns.

Fig. 12　Al concentration dependence on the Ag lattice parameter.

Fig. 13　Al concentration dependence on the Cu lattice parameter.

Fig. 14　(a)–(e) Schematic mechanism for the formation reaction of TiN layer at the interface between Ti-containing metal layer and AlN. (a) Diffusion of Ti and *M* into the AlN surface. (b) Co-generation of TiN particles and Al–*M* liquid phase by equation (2) and (3). (c, d) Growth of TiN layer toward the AlN inside and solidification of Al–*M* liquid phase by equation (4) and (5), and finally (e) TiN layer containing *M*-Al solid phase with Al concentration distribution following complete solidification of grain boundaries.

Table 1
The concentration of impurities related to the present work in Ag, Cu and TiH_2 powders by GD–MS.

Table 2
Compositional analysis of Ag phase in the TiN layer after brazing/ sintering for 30 min at 850 °C as shown in Figs. 4 and 9.

Table 3
Compositional analysis of Cu phase in the TiN layer after brazing/ sintering for 30 min at 850 °C as shown in Figs. 4 and 11.

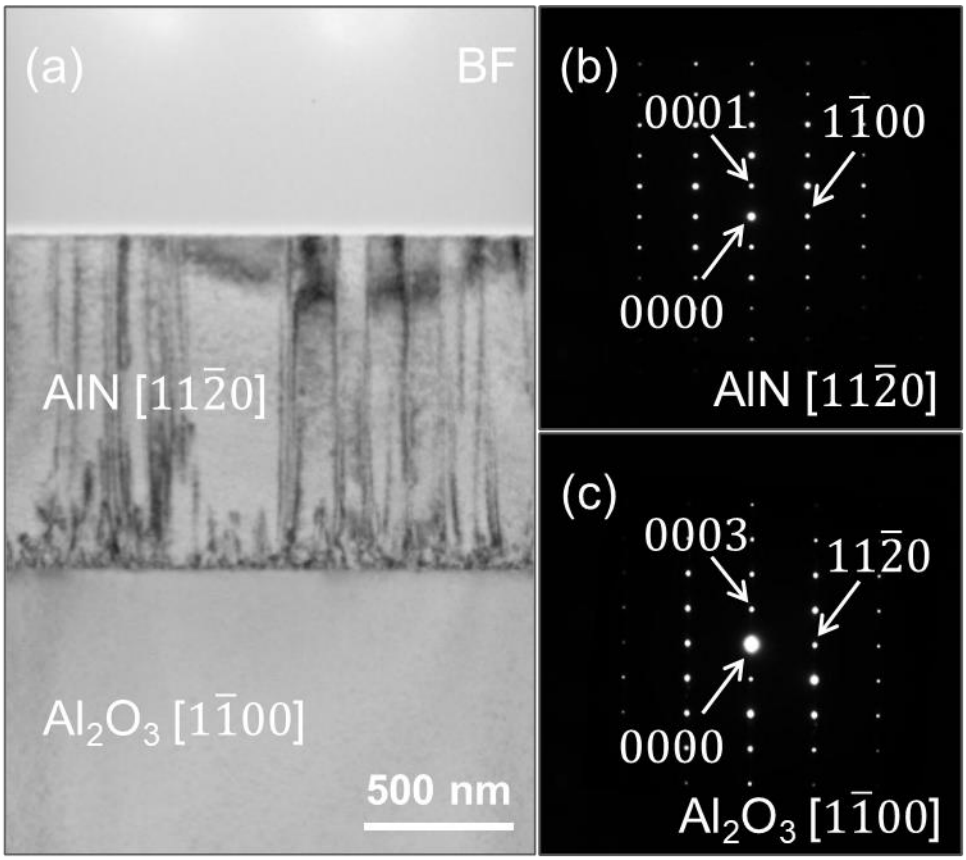

Fig. 1 (a) A cross-sectional BF TEM image of the AlN/ Al_2O_3 interface observed along the [11$\bar{2}$0] AlN zone axis, as shown in (b) in the selected area electron diffraction pattern. (c) election diffraction pattern with the incident electron beam parallel to [11$\bar{2}$0] AlN// [1$\bar{1}$00] Al_2O_3.

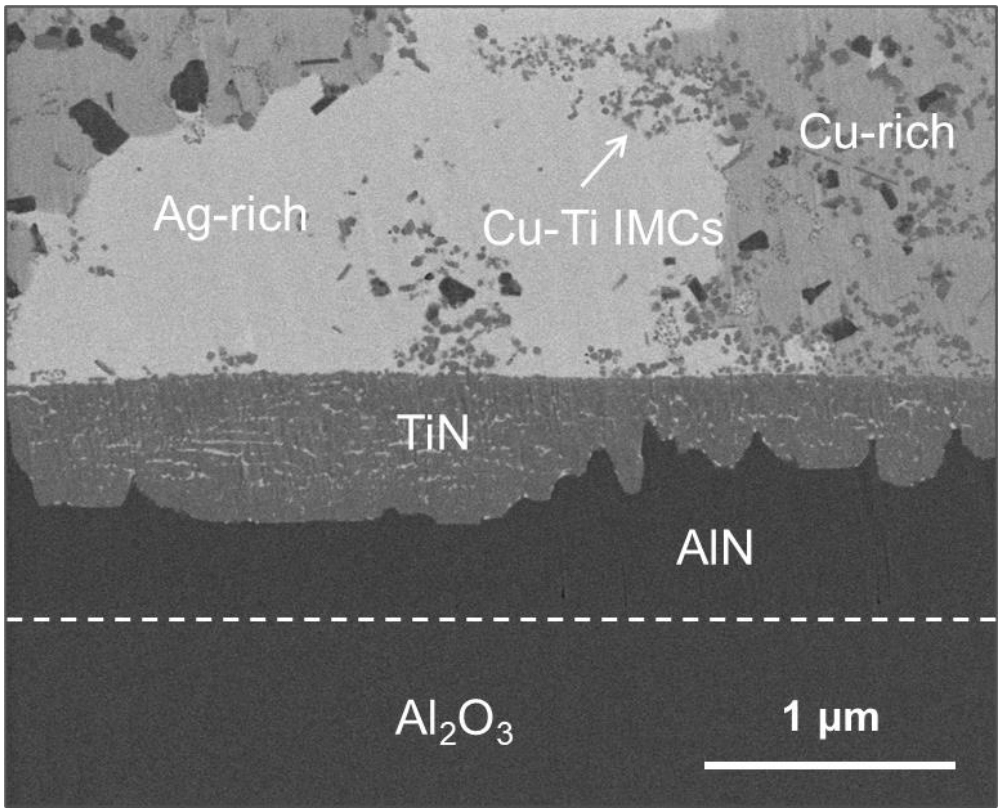

Fig. 2 SE image of chemical reaction products at a Ag–Cu–TiH_2/AlN interface after brazing for 30 min at 850 °C.

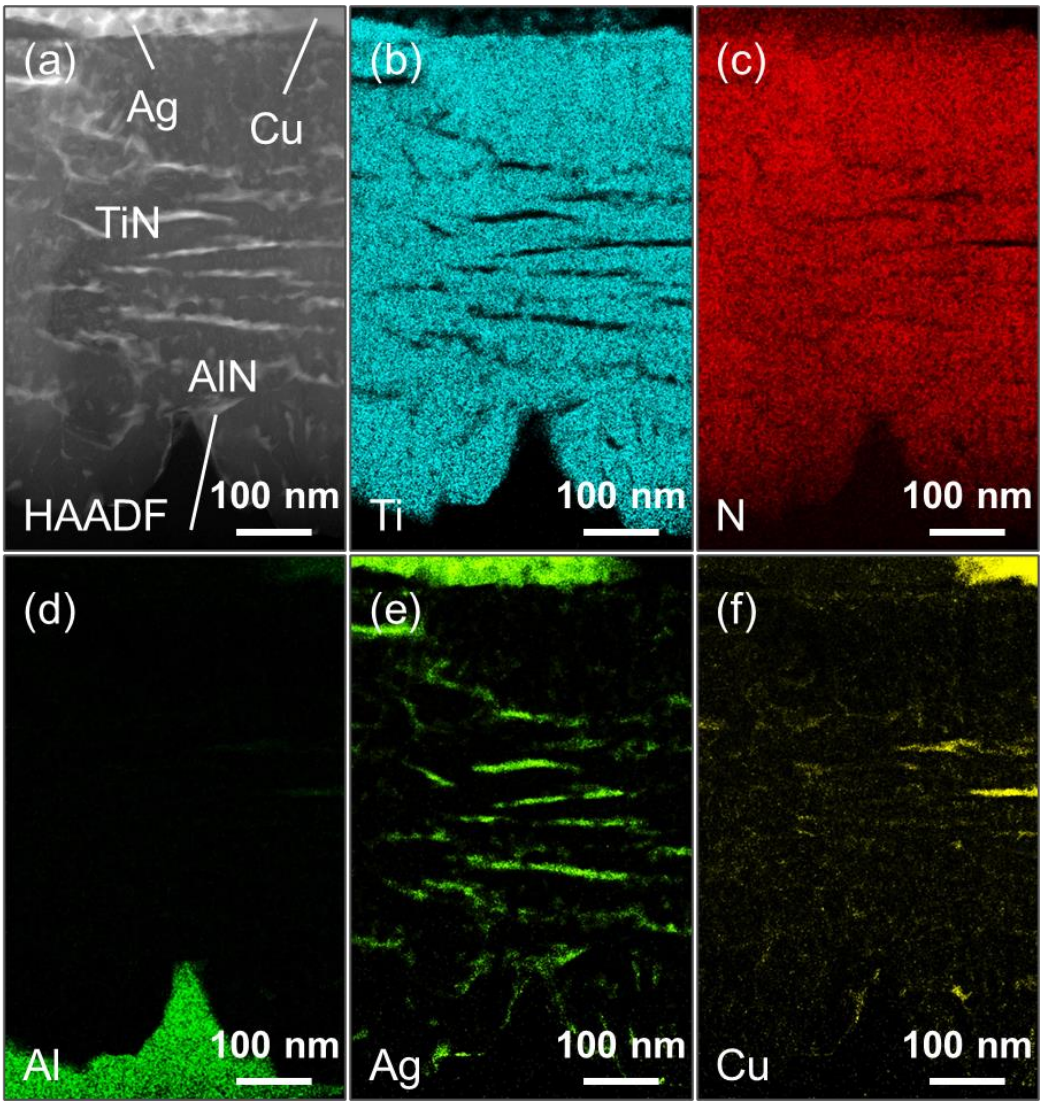

Fig. 3 (a) HAADF image of a Ag–Cu–TiH_2/AlN interface after brazing for 30 min at 850 °C, together with elemental distributions of (b) Ti, (c) N, (d) Al, (e) Ag and (f) Cu obtained by energy dispersive X-ray spectroscopy (EDS).

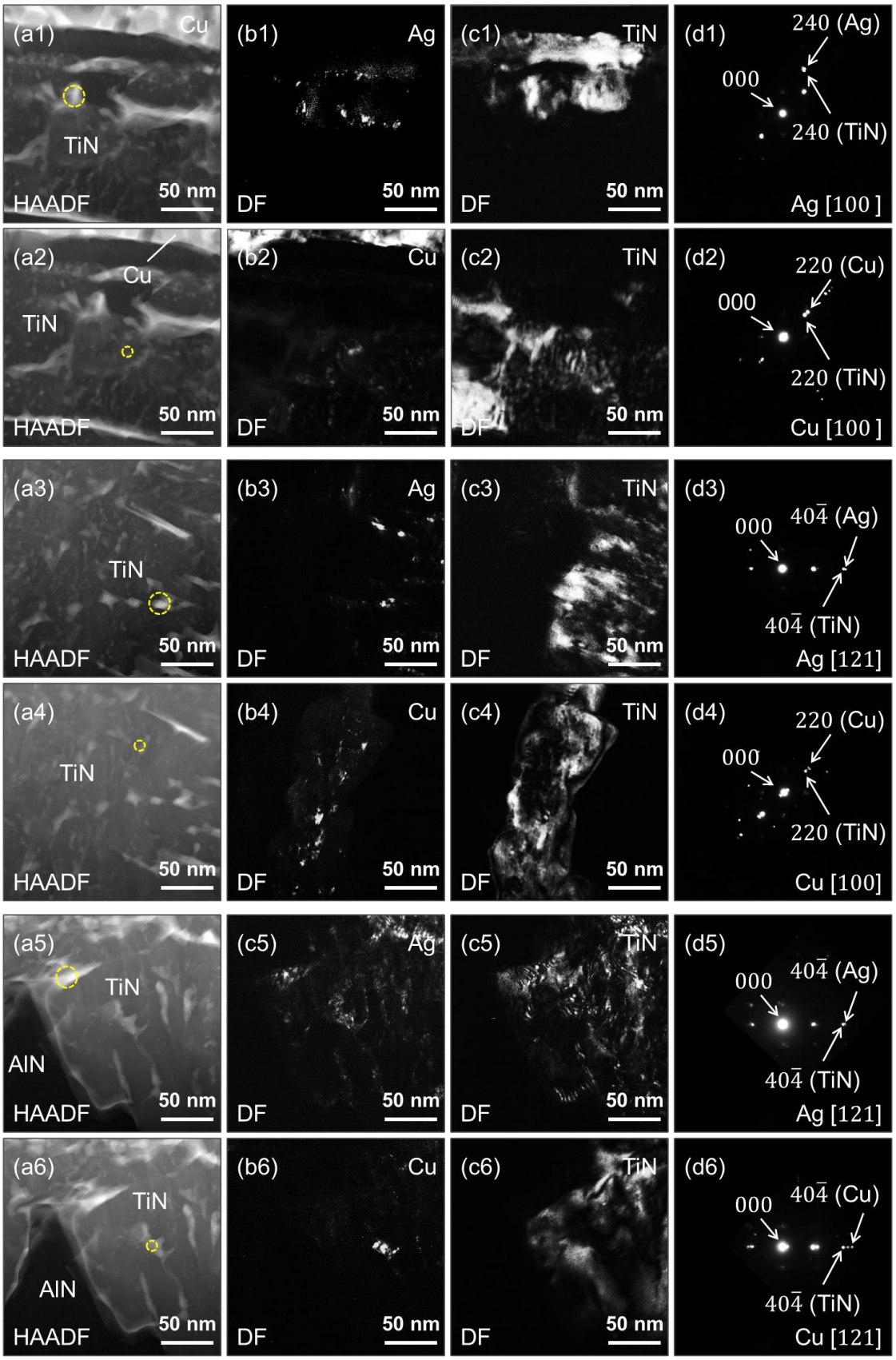
(a1)
Cu
TiN
HAADF
50 nm
(b1)
Ag
DF
50 nm
(c1)
TiN
DF
50 nm
(d1)
240 (Ag)
000
240 (TiN)
Ag [100]
(a2)
Cu
TiN
HAADF
50 nm
(b2)
Cu
DF
50 nm
(c2)
TiN
DF
50 nm
(d2)
220 (Cu)
000
220 (TiN)
Cu [100]
(a3)
TiN
HAADF
50 nm
(b3)
Ag
DF
50 nm
(c3)
TiN
DF
50 nm
(d3)
000
$40\bar{4}$ (Ag)
$40\bar{4}$ (TiN)
Ag [121]
(a4)
TiN
HAADF
50 nm
(b4)
Cu
DF
50 nm
(c4)
TiN
DF
50 nm
(d4)
220 (Cu)
000
220 (TiN)
Cu [100]
(a5)
TiN
AlN
HAADF
50 nm
(c5)
Ag
DF
50 nm
(c5)
TiN
DF
50 nm
(d5)
000
$40\bar{4}$ (Ag)
$40\bar{4}$ (TiN)
Ag [121]
(a6)
TiN
AlN
HAADF
50 nm
(b6)
Cu
DF
50 nm
(c6)
TiN
DF
50 nm
(d6)
000
$40\bar{4}$ (Cu)
$40\bar{4}$ (TiN)
Cu [121]

Fig. 4　(a1-6) HAADF images of a Ag–Cu–TiH_2/AlN interface after brazing for 30 min at 850 °C, (b1, 3, 5) DF images for Ag, (b2, 4, 6) for Cu and (c1-6) for TiN using $\boldsymbol{g}$ vectors as shown in the (d1-6) electron diffraction patterns. The HAADF images are grouped into three pairs: a1 and a2, a3 and a4, a5 and a6. Slight tilts in specimen orientation within each pair of HAADF images changes the electron diffraction patterns, as shown in d1 and d2, d3 and d4, d5 and d6. Examples of Ag- and Cu-containing areas in the HAADF images are circled.

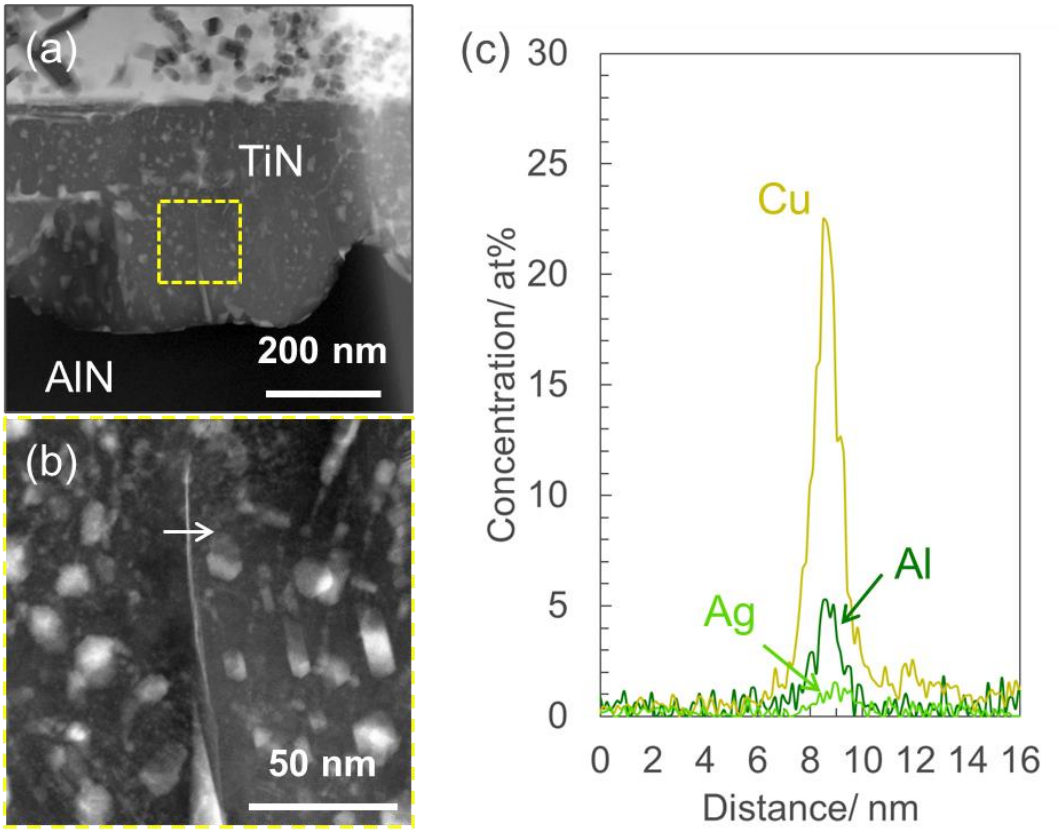

Fig. 5 (a, b) HAADF images of a Ag–Cu–TiH_2/AlN interface after brazing for 30 min at 850 °C, and (c) EDS analysis along the direction arrowed in (b).

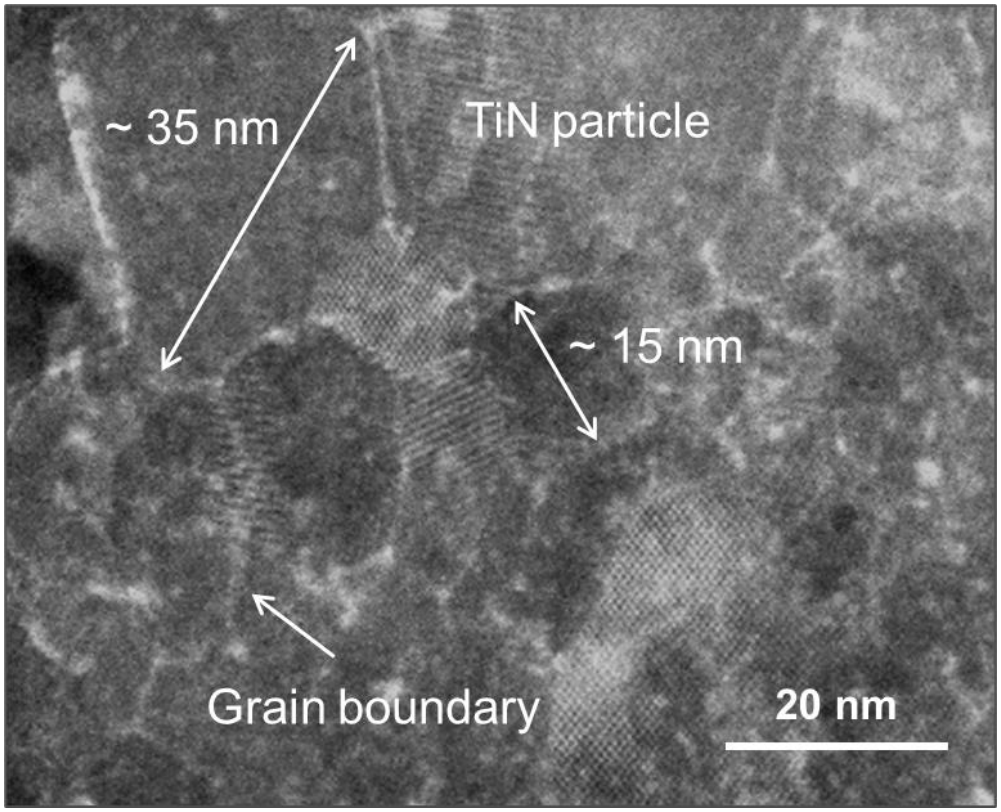

Fig. 6 Detailed HAADF image of TiN layer of a Ag–Cu–TiH_2/AlN interface after brazing for 30 min at 850 °C.

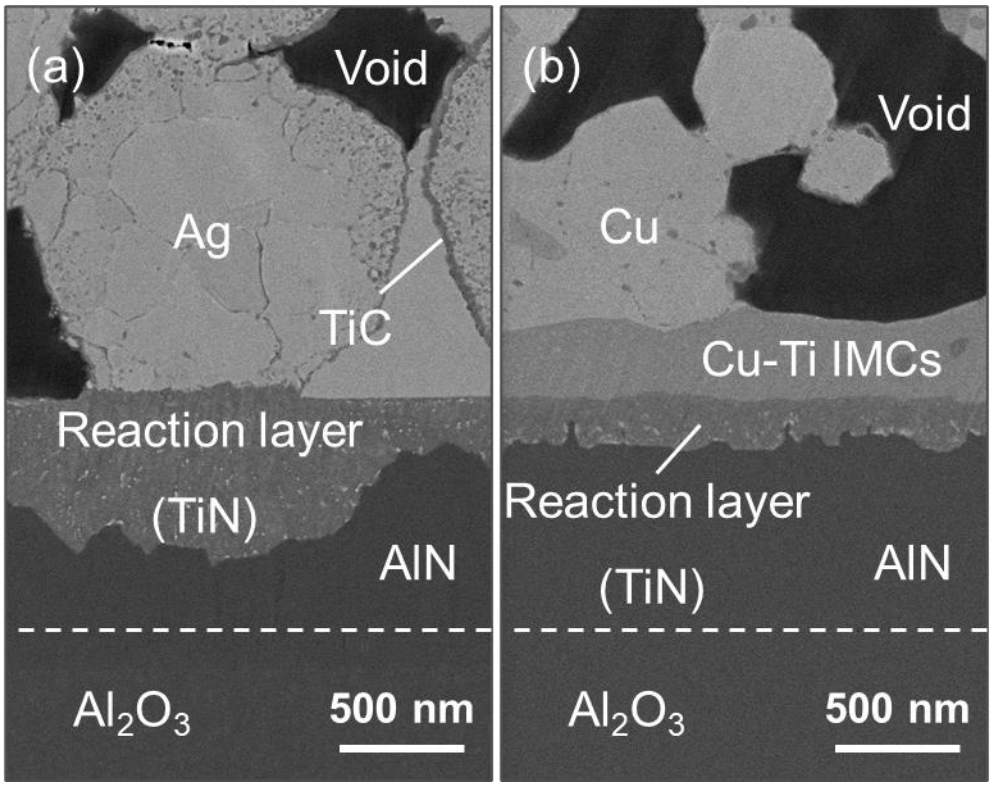

Fig. 7 SE images of chemical reaction products at (a) a Ag–TiH_2/AlN interface after sintering for 30 min at 850 °C, and (b) a Cu–TiH_2/AlN interface after sintering for 30 min at 850 °C.

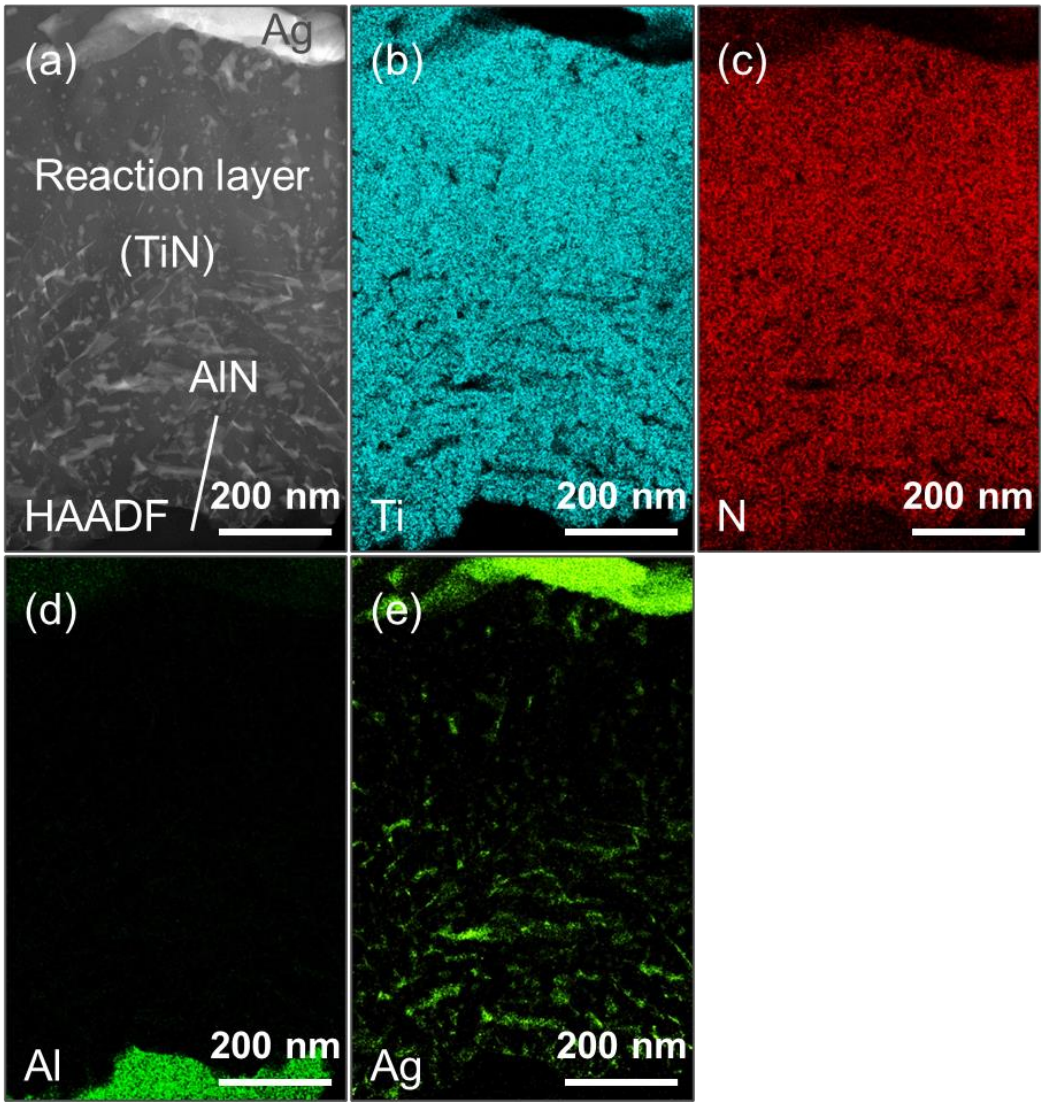

Fig. 8 (a) HAADF image of a Ag–TiH_2/AlN interface after sintering for 30 min at 850 °C, together with elemental distributions of (b) Ti, (c) N, (d) Al and (e) Ag obtained by EDS.

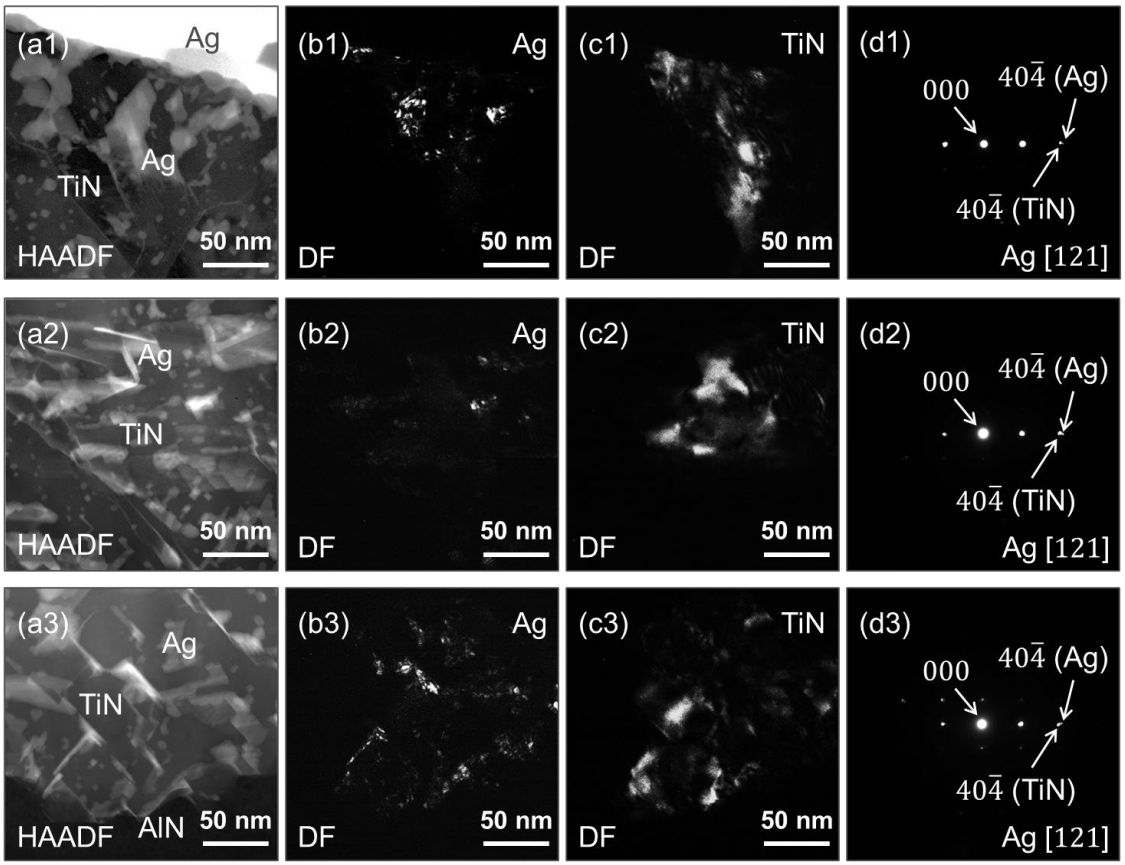

Fig. 9 (a1-3) HAADF images of a Ag–TiH_2/AlN interface after sintering for 30 min at 850 °C, (b1-3) DF images for Ag and (c1-3) for TiN using $\boldsymbol{g}$ vectors as shown in (d1-3) SAED patterns.

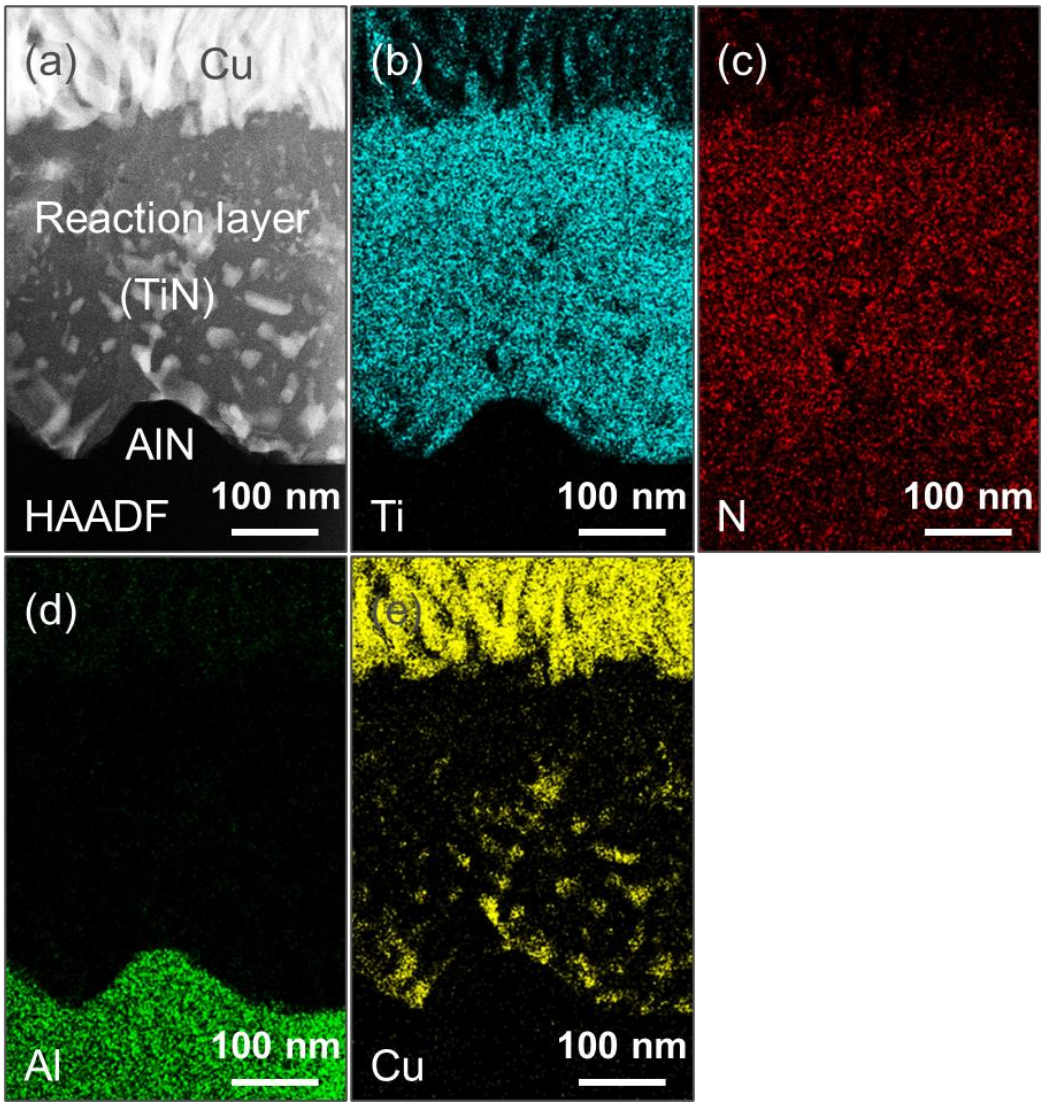

Fig. 10 (a) HAADF image of a Cu–TiH_2/AlN interface after sintering for 30 min at 850 °C, together with elemental distributions of (b) Ti, (c) N, (d) Al and (e) Cu obtained by EDS.

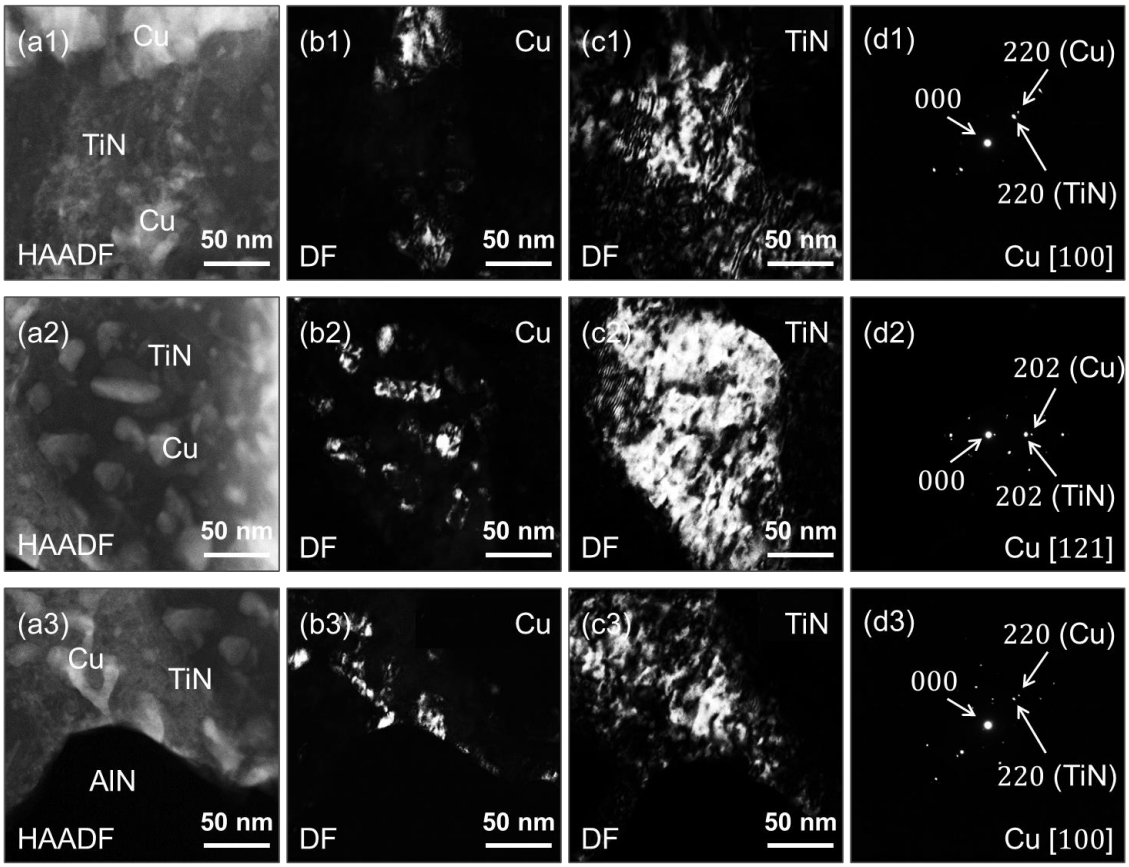

Fig. 11 (a1-3) HAADF images of a Cu–TiH_2/AlN interface after sintering for 30 min at 850 °C, (b1-3) DF image for Cu and (c1-3) for TiN using $\boldsymbol{g}$ vectors as shown in (d1-3) SAED patterns.

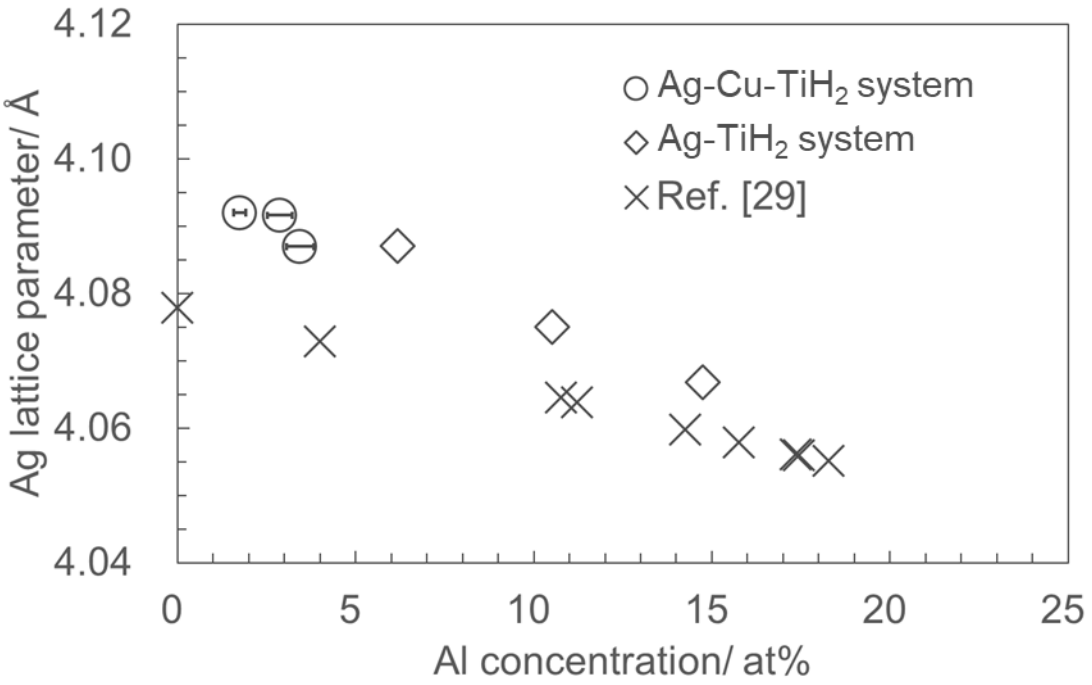

Fig. 12　Al concentration dependence on the Ag lattice parameter.

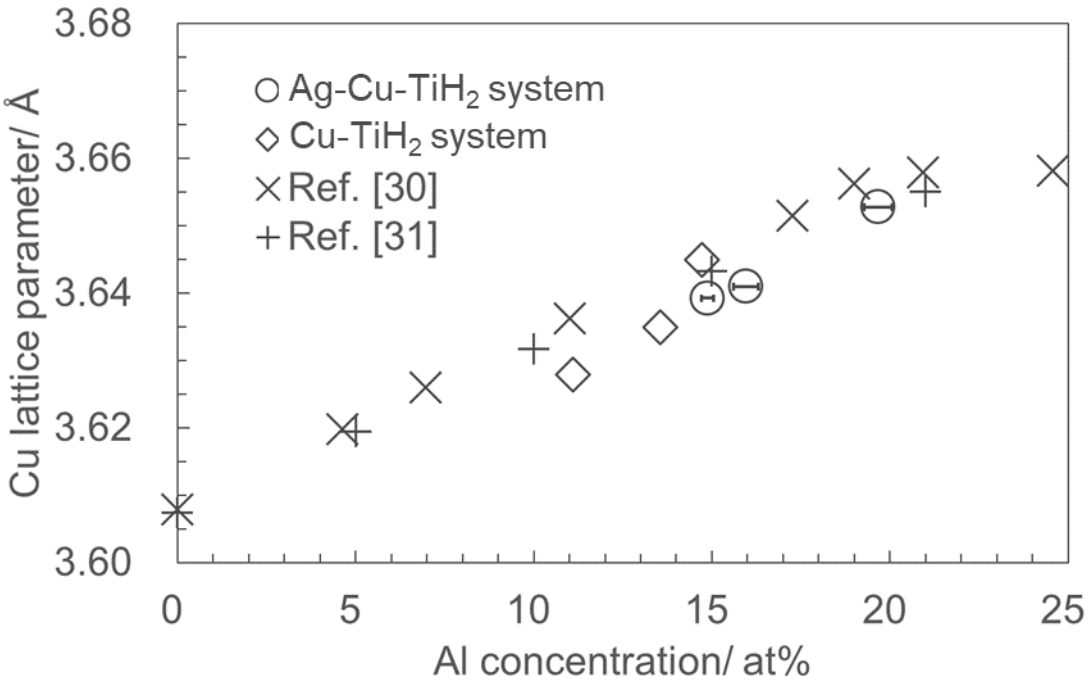

Fig. 13　Al concentration dependence on the Cu lattice parameter.

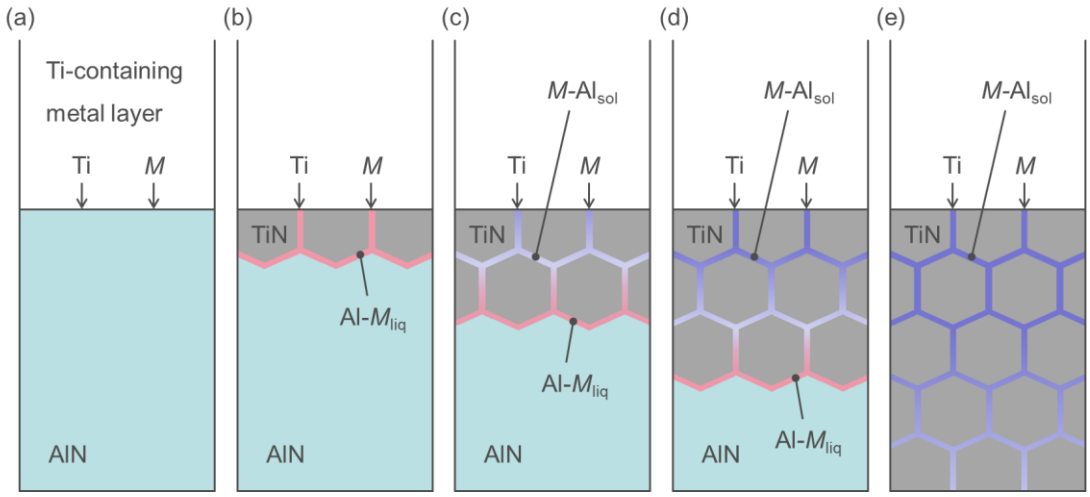

Fig. 14　(a)–(e) Schematic mechanism for the formation reaction of TiN layer at the interface between Ti-containing metal layer and AlN. (a) Diffusion of Ti and *M* into the AlN surface. (b) Co-generation of TiN particles and Al–*M* liquid phase by equation (2) and (3). (c, d) Growth of TiN layer toward the AlN inside and solidification of Al–*M* liquid phase by equation (4) and (5), and finally (e) TiN layer containing *M*-Al solid phase with Al concentration distribution following complete solidification of grain boundaries.

Powder	Concentration (wtppm)			
	Ag	Cu	Ti	Al
Ag	-	0.3	< 0.01	0.3
Cu	9.8	-	< 0.01	< 0.01
TiH_2	6.1	39	-	60

Table 1

The concentration of impurities related to the present work in Ag, Cu and TiH_2 powders by GD–MS.

Sample	Position in the TiN layer	Concentration (at%)					Al / (Al+Ag(+Cu)) (at%)
		Ag	Cu	Ti	Al	N	
Ag-Cu-TiH_2/ AlN	Metal layer side	46.7	10.2	15.9	0.9	26.3	1.9 (1.6)
	Center	41.6	11.9	17.1	1.4	28.0	3.2 (2.5)
	AlN side	17.8	4.7	35.4	0.7	41.4	3.8 (3.1)
Ag-TiH_2/ AlN	Metal layer side	30.3	-	37.3	2.0	30.4	6.2
	Center	23.7	-	42.3	2.8	31.2	10.5
	AlN side	14.3	-	47.4	2.5	35.8	14.7

Table 2

Compositional analysis of Ag phase in the TiN layer after brazing/ sintering for 30 min at 850 °C as shown in Figs. 4 and 9.

Sample	Position in the TiN layer	Concentration (at%)					$\frac{Al}{Al+Cu(+Ag)}$ (at%)
		Ag	Cu	Ti	Al	N	
Ag-Cu-TiH_2/ AlN	Metal layer side	0.7	23.6	38.7	4.2	32.7	15.1 (14.7)
	Center	0.3	17.1	40.7	3.3	38.7	16.1 (15.8)
	AlN side	9.4	34.5	19.7	9.5	26.9	21.6 (17.8)
Cu-TiH_2/ AlN	Metal layer side	-	25.6	39.3	3.2	31.9	11.1
	Center	-	40.0	28.0	6.3	25.7	13.4
	AlN side	-	65.5	10.8	11.3	12.3	14.9

Table 3

Compositional analysis of Cu phase in the TiN layer after brazing/ sintering for 30 min at 850 °C as shown in Figs. 4 and 11.

Supplemental Material

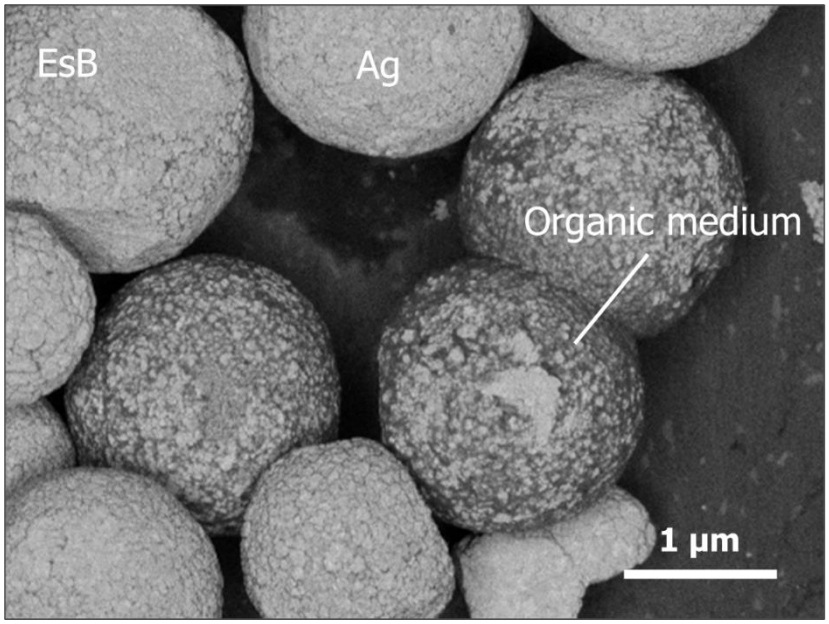

Fig. S1　Surface EsB (energy selective backscattered electron) image of the Ag powder used in this work.

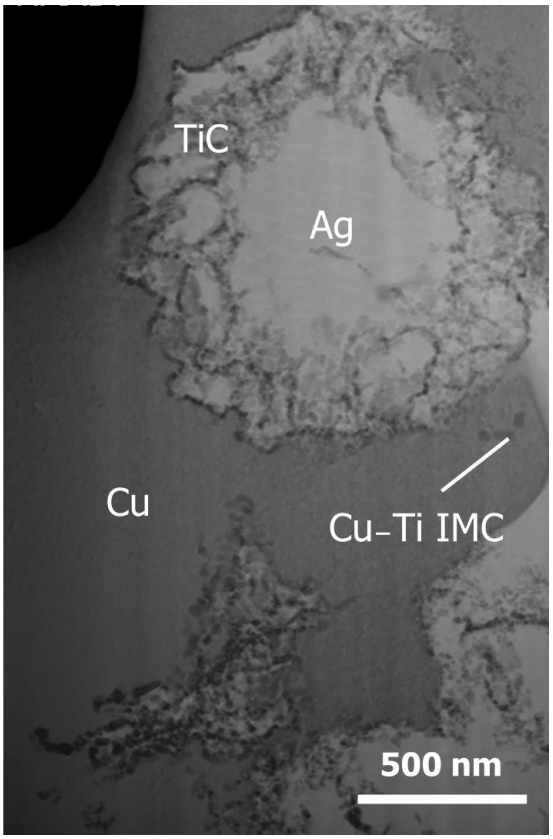

Fig. S2 Cross-sectional HAADF image of a Ag–Cu alloy layer in the Ag–Cu–TiH_2 system after brazing for 30 min at 850 °C.

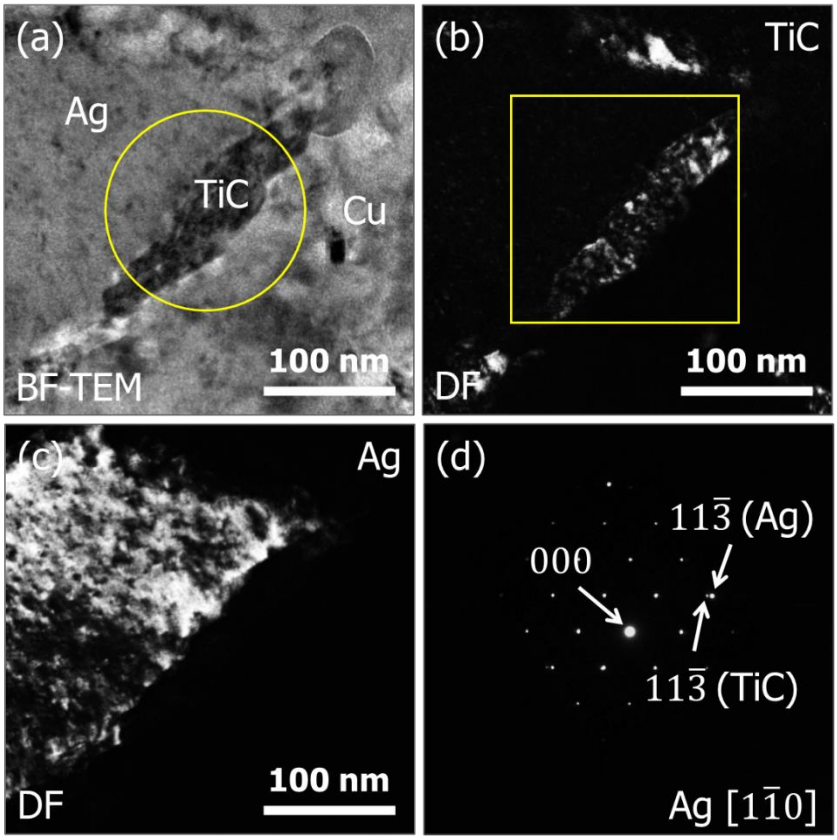

Fig. S3 (a) BF-TEM image of a TiC particle in the Ag–Cu–TiH_2 system after brazing for 30 min at 850 °C, (b) DF image for TiC and (c) for Ag using $\boldsymbol{g}$ vectors as shown in (d) SAED pattern. This SAED pattern was acquired from the yellow circle shown in (a).

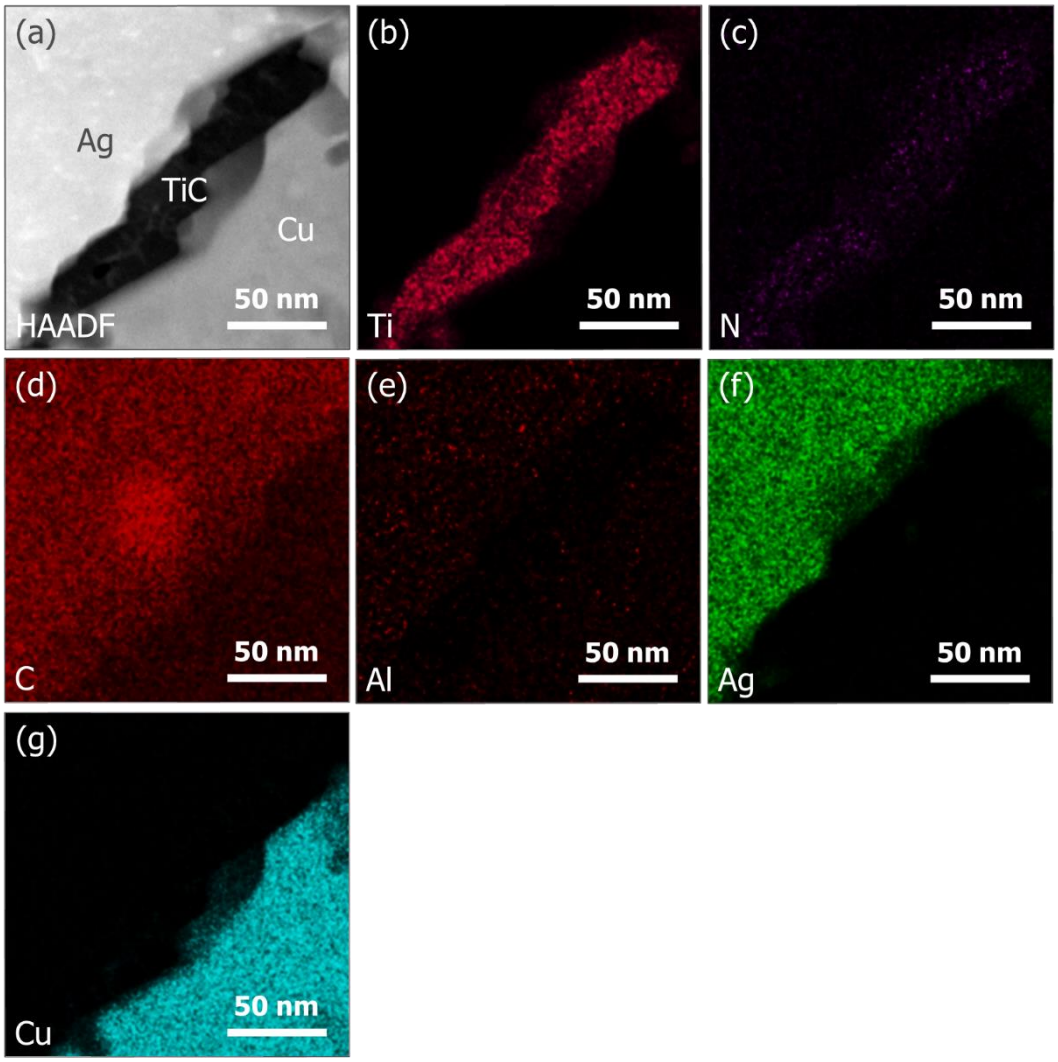

Fig. S4　(a) HAADF image of a TiC particle in the Ag–Cu–TiH_2 system after brazing for 30 min at 850 °C, together with elemental distributions of (b) Ti, (c) N, (d) C, (e) Al, (f) Ag and (g) Cu obtained by EDS from the yellow selected area shown in Fig. S3 (b).

	Concentration/ at%					
	C	N	Al	Ti	Cu	Ag
TiC	58.2	0.0	0.3	38.4	2.6	0.4
Ag	58.7	0.0	1.6	0.1	1.5	38.2
Cu	12.6	0.0	0.9	1.1	85.1	0.3

Table. S1 Compositional analysis of chemical products of a Ag—Cu alloy layer in the Ag–Cu–TiH_2 system after brazing for 30 min at 850 °C as shown in Fig. S4 (a). The high apparent C concentration in Ag is due to the proximity of the Ag–Mα and C–Kα lines.